



HAL
open science

Electrostatic Directed Assembly of Colloidal Microparticles Assisted by Convective Flow

Lauryanne Teulon, Yannick Hallez, Simon Raffy, François Guerin, Etienne
Palleau, Laurence Ressler

► **To cite this version:**

Lauryanne Teulon, Yannick Hallez, Simon Raffy, François Guerin, Etienne Palleau, et al.. Electrostatic Directed Assembly of Colloidal Microparticles Assisted by Convective Flow. *Journal of Physical Chemistry C*, 2019, 123 (1), pp.783-790. 10.1021/acs.jpcc.8b08981 . hal-02284270

HAL Id: hal-02284270

<https://hal.science/hal-02284270v1>

Submitted on 11 Sep 2019

HAL is a multi-disciplinary open access archive for the deposit and dissemination of scientific research documents, whether they are published or not. The documents may come from teaching and research institutions in France or abroad, or from public or private research centers.

L'archive ouverte pluridisciplinaire **HAL**, est destinée au dépôt et à la diffusion de documents scientifiques de niveau recherche, publiés ou non, émanant des établissements d'enseignement et de recherche français ou étrangers, des laboratoires publics ou privés.





Open Archive Toulouse Archive Ouverte (OATAO)

OATAO is an open access repository that collects the work of Toulouse researchers and makes it freely available over the web where possible

This is an author's version published in: <http://oatao.univ-toulouse.fr/24214>

Official URL: <https://doi.org/10.1021/acs.jpcc.8b08981>

To cite this version:

Teulon, Lauryanne and Hallez, Yannick  and Raffy, Simon  and Guerin, François and Palleau, Etienne and Ressler, Laurence *Electrostatic Directed Assembly of Colloidal Microparticles Assisted by Convective Flow*. (2019) *Journal of Physical Chemistry C*, 123 (1). 783-790. ISSN 1932-7447

Any correspondence concerning this service should be sent to the repository administrator: tech-oatao@listes-diff.inp-toulouse.fr

Electrostatic Directed Assembly of Colloidal Microparticles Assisted by Convective Flow

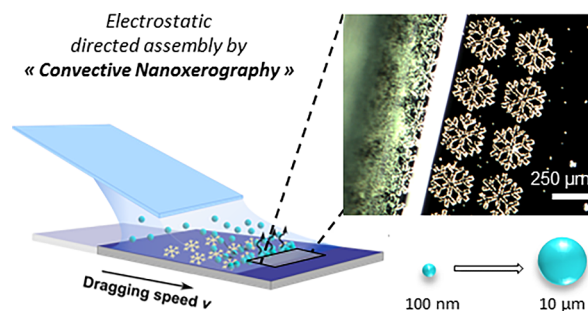
Lauryanne Teulon,[†] Yannick Hallez,[‡] Simon Raffy,[†] François Guerin,[†] Etienne Palleau,[†] and Laurence Ressler^{*,†}

[†]LPCNO, Université de Toulouse, CNRS, INSA, UPS, 135 Avenue de Rangueil, 31077 Toulouse, France

[‡]Laboratoire de Génie Chimique, Université de Toulouse, CNRS, INPT, UPS, Toulouse, France

Supporting Information

ABSTRACT: Electrostatic directed assembly of colloidal particles on charged patterns, that is, nanoxerography, has proven to find innovative applications in plasmonics, anticounterfeiting, or particle sorting. However, this technique was restricted to dispersions of nanoparticles whose diameters are typically below 100 nm. The combination of experiments and simulations shows that this limitation is due to an uncontrolled dewetting of the substrate and to the low mobility of large particles. The “convective nanoxerography” process developed in this work overcomes this limit and allows making selective and dense assemblies of micrometer-sized particles expanding by a factor 40 the size range foreseeable.



INTRODUCTION

Methods to direct the assembly of colloidal particles on flexible or solid substrates have been developed^{1–6} over the past decades in order to benefit from their original properties (mechanical, optical, and chemical...) into functional devices. Among all the existing directed assembly methods, the nanoxerography technique, based on the trapping of charged or polarizable particles on an electrostatically patterned substrate, offers the possibility to make 1D to 3D^{7–10} particle assemblies with high resolution in a few seconds. Applications were found in plasmonics,¹¹ anti-counterfeiting,^{7,12} or particle sorting.¹³ Interestingly, when considering nanoxerography of objects with at least one dimension above 500 nm, very little work has been done and it has been mainly related to highly anisotropic objects with one small dimension,^{10,14} or particles dispersed in nonpolar solvents.^{15,16} Particle patterns were not precisely defined otherwise. Besides, few theoretical works have been devoted to describe the kinetics of particle assemblies by nanoxerography.

In this work, an improved method named “convective nanoxerography” has been developed in combination to numerical simulations to understand and overcome the limits of nanoxerography for micrometer-sized particle assemblies.

EXPERIMENTAL SECTION

Conventional Nanoxerography Process. Figure 1a presents the process of conventional nanoxerography, composed of two steps (i) and (ii):

- (i) The electrostatic charge writing step onto a polymethylmetacrylate (PMMA)¹⁸ thin film. In the frame of this work, this step was carried out by electric microcontact

printing (e- μ CP):¹⁷ a 25 mm² network of 250 μ m width, positively charged snowflake patterns were generated by putting into contact an electrically polarized flexible stamp featuring the snowflake structures with the PMMA thin film. Details on the e- μ CP protocol are given in page S2 of the Supporting Information. The large global dimensions of the patterns (nevertheless including micrometric features), were chosen accordingly to match with the full size range of particles (100 nm to 10 μ m) to be assembled.

- (ii) The development step which consists in immersing the charged substrate in the colloidal dispersion of interest during a “static” contact time t_{sc} (typically 5–45 s), followed by a manual withdrawal of the substrate and a subsequent natural drying in air. “Dynamic” contact time t_{dc} is defined as the sum of the time required for pulling the substrate out of the dispersion and the time required for drying the residual thin film of the solvent. t_{dc} is typically a few seconds only. This process ends with colloidal particles electrostatically and selectively assembled onto the charged patterns. In this study, negatively charged latex particles (carboxylate functionalized, fluorescent) dispersed in isopropanol (IPA) solvent at a typical concentration range of 10⁸ particles per mL, were chosen as model particles to be assembled on positively charged patterns.

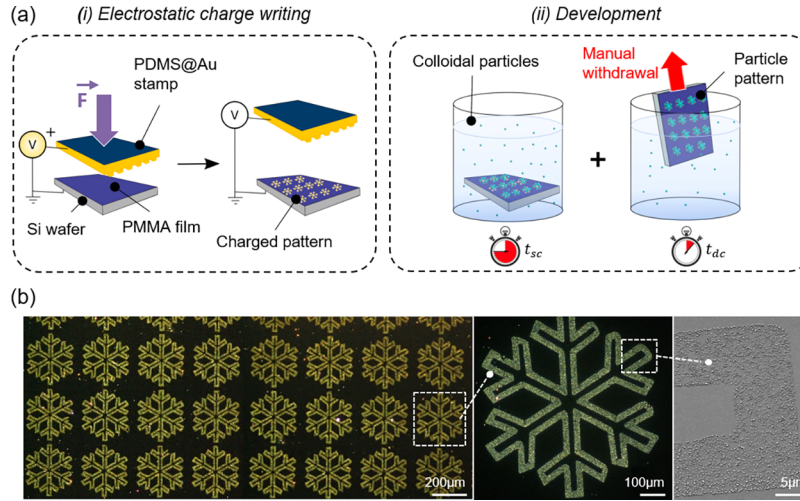


Figure 1. (a) Schematic representation of the conventional nanoxerography process with electrostatic charge writing using $e\text{-}\mu\text{CP}$ and development by manual immersion with a static contact time t_{sc} and a dynamic contact time t_{dc} . (b) dark field optical microscopy images of a 100 nm latex particle assembly forming snowflake patterns obtained by nanoxerography with $t_{sc} = 30$ s, $t_{dc} = 1\text{--}2$ s, $\rho_b = 4.55 \times 10^{10}$ mL $^{-1}$, $\Psi_s \approx 2$ V in air (left and middle); and zoom-in on a pattern by scanning electron microscopy (right).

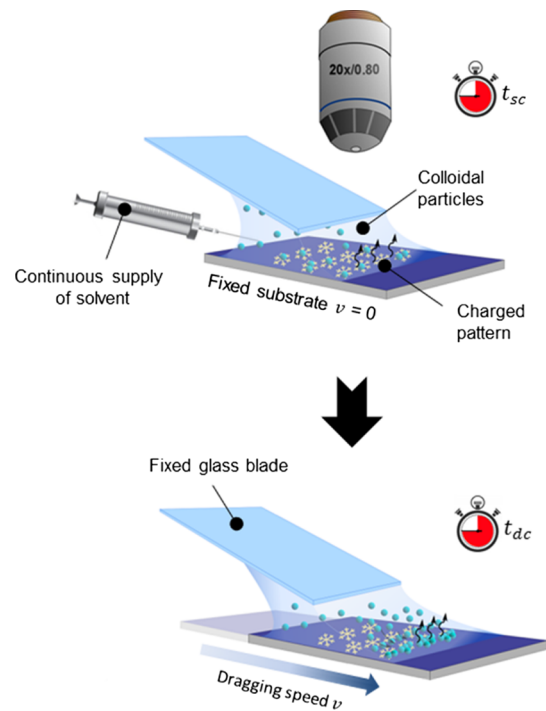
By adjusting the bulk colloidal dispersion density ρ_b , t_{sc} and the surface potential of the charged patterns Ψ_s , the nanoxerography technique allows directing the assembly of a wide range of submicrometer colloidal particles.^{7,10,19} As an example, monolayered assemblies of 100 nm latex particles were performed by nanoxerography with a good “pattern density” ρ_p (average surface density of particles deposited on charged patterns) and a good “selectivity” defined as $S = 1 - \rho_{bg}/\rho_p$ in our fixed-pattern geometry, where ρ_{bg} is the average surface density of particles deposited outside charged patterns (Figure 1b). Note that we consider the pattern density to be good when the particle pattern is clearly identifiable (in the Figure 1b case, $\rho_p = 6.6 \times 10^6$ mm $^{-2}$). Furthermore the selectivity is considered to be good when the pattern is easily distinguishable from the background which implies that S has to be superior to 0.8 (in the Figure 1b case, $S > 0.9$).

As previously mentioned, nanoxerography has been rarely applied to dispersions of micrometer-sized particles. However, understanding and tackling this size limitation would allow enlarging the capabilities of the technique and giving insights in the corresponding assembly kinetics. To investigate it, 1 μm latex particle assembly trials were carried out using the nanoxerography protocol described above. The solution was manually stirred for a few seconds before the development step. It appears that a static contact time at least 10 times longer than the one used for 100 nm particle assemblies was required in combination with a slow and careful manual withdrawal of the substrate to start obtaining some 1 μm particle assemblies but their density and selectivity were very poor (Supporting Information, Figure S1). Indeed, inhomogeneous dewetting of the substrate occurs during uncontrolled solvent evaporation, leading, sometimes, to particle aggregation at locations uncorrelated to those of charged patterns. This example reveals that both t_{sc} and the way the solvent evaporates strongly impact microparticle assemblies by nanoxerography.

Convective Nanoxerography Process. To gain new insights into the key mechanisms involved in the nanoxerography assembly of micrometric particles, a better control over solvent evaporation was required. Therefore, instead of immersing the whole charged substrate in a colloidal dispersion

bath, a 10–15 μL drop of the colloidal dispersion was deposited on the substrate for an initial period of time t_{sc} . The meniscus formed by the dispersion drop on the substrate was then dragged by translating a temperature regulated stage (20 $^{\circ}\text{C}$) at a fixed speed v , called the dragging speed (between 5 and 100 $\mu\text{m}\cdot\text{s}^{-1}$) under a fixed glass blade (Scheme 1). A camera mounted on a vertical optical microscope positioned just above the glass blade allowed recording real-time videos of the particle-assembly kinetics. All experiments were conducted at a constant ambient

Scheme 1. Schematic Representation of the Convective Flow Development with an Initial Period of Static Contact Time t_{sc} with a Motionless Substrate, and a Second Step of Meniscus Dragging by Substrate Translation at the Dragging Speed v Associated to a Dynamic Contact Time t_{dc}



temperature of 20 °C and a humidity ratio of 40%. More details on the set up are reported in [Supporting Information](#) pages S3 and S4.

RESULTS AND DISCUSSION

Assembly Mechanisms in Conventional Nanoxerography Applied to 1 μm Particles. The application of the conventional nanoxerography process in the case of 1 μm particles is reported in [Figure 2a](#). Note that to gain

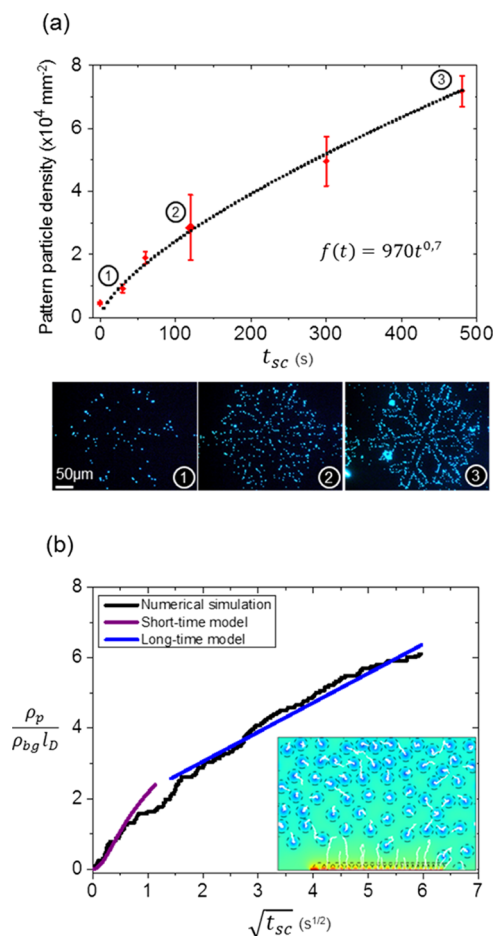


Figure 2. (a) Pattern particle density as a function of the static contact time t_{sc} with a dragging speed of $80 \mu\text{m}\cdot\text{s}^{-1}$ ($t_{dc} = 31 \text{ s}$) and fluorescent optical microscopy images of corresponding assemblies. (b) Scaled pattern particle density as a function of $\sqrt{t_{sc}}$ in nanoxerography simulations (black); short-time model (3) (violet); long-time model (4) (blue). Inset: simulated dimensionless potential ψ (colormap) and particle trajectories (white lines) at the final time. Dashed lines materialize a distance l_D around particles. $\rho_b = 6.825 \times 10^8 \text{ mL}^{-1}$ in every experiment and simulation.

reproducibility the set up described in [Scheme 1](#) was used here for the development step but with a high dragging speed v fixed at $80 \mu\text{m}\cdot\text{s}^{-1}$ to mimic a manual withdrawing of the substrate. The particle concentration ρ_b was adjusted here at $6.825 \times 10^8 \text{ mL}^{-1}$ (in comparison to $\rho_b = 4.55 \times 10^{10} \text{ mL}^{-1}$ in the 100 nm nanoparticle case) so that the surface-covering concentration (defined as the concentration of particles in $\text{Ps}\cdot\text{mL}^{-1}$ multiplied by the covering surface—or surface section—of a single particle) is identical for each particle size case. The pattern density of monolayered assemblies was measured from microscope images obtained as detailed in [Supporting](#)

[Information](#) (Figures S2 and S3). For vanishing static contact times, the snowflake pattern is barely identifiable, whereas a good pattern-particle density ($\rho_p > 5 \times 10^4 \text{ mm}^{-2}$) is obtained for $t_{sc} = 480 \text{ s}$ as shown on fluorescent images ([Figure 2a](#)).

The experimental increase of particle density on a charged pattern observed as a function of t_{sc} can be fitted with a function $f(t) = At^b$, where $A = 970 \pm 192 \text{ Ps}\cdot\text{mm}^{-2}\cdot\text{s}^{-1}$ and $b = 0.70 \pm 0.04$. Similar experiments on 500 nm latex nanoparticles yielded $b = 0.40 \pm 0.01$ ([Supporting Information](#), Figure S8). This trend close to \sqrt{t} suggests that assembly kinetics may be dictated by a diffusion mechanism. These results seem to indicate that to overcome the nanoxerography limitation for large particles, a long period of time is at least required for particles to move toward the charged patterns by diffusion before electrostatics take over at short distances from the substrate.

To confirm and improve our mechanism analysis, mean-field Brownian dynamics (BD) simulations^{20,21} were undertaken. For each simulation, a few tens of particles of diameter $d = 1 \mu\text{m}$ were randomly placed in a 3D numerical domain of dimensions $L_x \times L_y \times L_z = 300 \times 200 \times 2 \mu\text{m}^3$ and a charged pattern of length $L_p = 200 \mu\text{m}$ was introduced at the bottom of this domain. The particle positions were derived with a standard BD algorithm. The electrostatic forces exerted on each particle were computed by integration of the excess osmotic stress tensor on their surface. The latter is a function of the electrostatic potential field which is obtained in general by solving the Poisson–Boltzmann (PB) equation. When the electrostatic potential is moderate (less than about 40 mV), this equation can be linearized and is known as the Debye–Hückel (DH) equation

$$\Delta\psi = \kappa^2\psi \quad (1)$$

where ψ is the electric potential scaled by kT/e , k is Boltzmann’s constant, $T = 293 \text{ K}$ is the absolute temperature, e is the unit charge, and κ is the inverse of the Debye length l_D . Even for highly charged surfaces, the DH equation is valid at large distances because of the decay of the potential. It can therefore match predictions of the nonlinear PB equation provided the boundary conditions are modified. For constant surface potentials, the latter are termed “effective” surface potentials. In the present work, both the particles and the substrate obey constant effective potential conditions. On the particle surface, it stems from a special case of charge regulation as shown in [Supporting Information](#) (see pages S7 and S8).²² An effective surface potential value $\psi_s = -3.41$ and an effective screening length $l_D \approx 10 \mu\text{m}$ were measured by electrophoresis. On the charged pattern, the constant effective potential condition $\psi_p \approx 4$ comes from the effective surface charge saturation phenomenon observed for very large surface charge densities.²³ The solution of the DH eq 1 with effective surface potential conditions is expected to be close to that of the full nonlinear PB theory with true surface potentials or charge densities when the distances between charged surfaces are larger than $O(l_D)$. The dispersions considered here are dilute everywhere but on the charged pattern so the particle layer structuration on the pattern is only qualitative but the migration of particles in the dispersion is quantitative.

The DH equation was solved numerically with a finite-difference scheme modified with the so-called level-set/ghost fluid method to enforce the boundary conditions on the moving surfaces of the particles. The grid used to discretize the space contained $1200 \times 800 \times 16$ cells, which was enough to obtain particle trajectories independent of the grid size. More details on the numerical solver can be found in refs.^{20,21}

Note that the experiments reported in Figure 2a were carried out pulling the stage at a speed of $80 \mu\text{m}\cdot\text{s}^{-1}$ and that convection was not included in the simulations. This is not a problem because at these large dragging speeds the hydrodynamic flow is parallel to the substrate, inducing advective flows of particles parallel to the substrate, whereas assembly on the substrate is driven by particle flows essentially normal to the substrate (diffusion and electrostatic repulsions).

Numerical results corresponding to the experimental conditions of Figure 2a are reported in Figure 2b. Here, the pattern density is scaled by $\rho_b l_D$. Note that because these simulations are quasi-2D, the electrostatic field generated by the charged pattern is stronger and longer-ranged than the experimental one, so the numerical value of ρ_p cannot be compared directly to its experimental counterpart. Simulations allow nonetheless to understand the mechanisms at play in the experiments. They reveal in particular the existence of two successive phases in the particle migration process, as shown in Figure 2b. These two regimes can be understood by considering the 1D transport equation for the particle density above a charged surface

$$\partial_t \rho = \partial_y (D(\rho) \partial_y \rho - \rho m F) \quad (2)$$

The “diffusion” term includes both the effects of Brownian motion and of particle–particle interactions through the collective diffusion coefficient $D(\rho)$ which can be computed from the generalized Stokes–Einstein relation and the PB cell model as detailed in Supporting Information page S9. The second term accounts for the migration of particles with mobility m due to the electrostatic force exerted by the charged substrate $F(y)$. Note that particle sedimentation is neglected in this model. This will be discussed hereafter.

During the first and fast phase, particles placed at a distance from the charged pattern comparable to or smaller than the screening length l_D interact with the charged substrate with an energy much larger than kT so the diffusion term in eq 2 is negligible compared to the migration term (see the quasi “ballistic” trajectories of these particles in the insert of Figure 2b). Using a Derjaguin–Landau–Verwey–Overbeek-like force model for F^{24} (Supporting Information, Figure S5), the solution of (eq 2) is

$$\rho = \rho_b \left(\frac{t}{\tau} e^{-y/l_D} + 1 \right)^{-1}$$

where $\tau = l_D / (mF(0))$ is the characteristic migration time over the distance of influence of electrostatics. Integrating in time the flux density $\rho m F$ evaluated on the substrate then yields the density of adsorbed particles at short times

$$\rho_p = \rho_b l_D \ln(1 + t/\tau) \quad (3)$$

The good agreement between this result and the simulation reported in Figure 2b supports the idea that particle transport is dominated by electrostatic effects in the first phase.

During the second phase, particle adsorption on the charged patterns is much slower as the particles remaining in the solvent must first diffuse toward the zone $y < l_D$ before being captured by electrostatic forces. Mass transport is thus dominated by diffusion in the region $y > l_D$ and the last term in eq 2 can be neglected. Calculations of the collective diffusion coefficient as reported in page S9 of Supporting Information lead to a quasi-constant value for the range of volume fractions investigated (D

$\in [220D_0, 245D_0]$) so the constant value $D(\rho_b)$ is used to solve (eq 2) with the classical result

$$\rho = \rho_b \operatorname{erf} \left(\frac{y}{2\sqrt{Dt}} \right)$$

Once again, time-integration of the resulting flux density at the substrate leads to the long-time result

$$\rho_p = 2\rho_b \sqrt{\frac{Dt}{\pi}} + \rho_0 \quad (4)$$

where ρ_0 is a constant depending on the adsorbed density at the beginning of the diffusive regime. This $t^{1/2}$ dependence is consistent with the experimental data presented in Figure 2a although the prefactor is different, as expected, because the real system is not 1D. On the other hand, the agreement with the BD simulations is excellent (blue line in Figure 2b) because of the quasi-1D geometry of the numerical experiment. Note in particular that the slope of the model curves is determined theoretically, without any fitting procedure. Other simulations undertaken with different bulk particle densities produced the same agreement.

Sedimentation was neglected both in simulations and in the model. During the first phase, this hypothesis is reasonable if the sedimentation velocity v_s is negligible compared to the migration velocity induced by the charged pattern, the latter being of order $mF(l_D)$. During the second phase, migration is induced by the density gradient resulting from the rapid condensation of particles close to the charged pattern. The associated migration velocity is $D(\rho) \partial_y \rho / \rho \approx D(\rho_p) / l_D$. For the system under consideration here, $v_s \approx 0.071 \mu\text{m}\cdot\text{s}^{-1}$, $mF(l_D) \approx 33 \mu\text{m}\cdot\text{s}^{-1}$, and $D(\rho_p) / l_D \approx 4.7 \mu\text{m}\cdot\text{s}^{-1}$ so neglecting sedimentation is indeed justified. Moreover, significant sedimentation phenomena would induce an adsorbed density increase proportional to t in experiments, which was not observed for $1 \mu\text{m}$ particles. Note however that sedimentation effects were identified by microscopy for 4.3 and $10 \mu\text{m}$ particles in the same physico-chemical conditions.

To summarize this section concerning the limits of conventional nanoxerography, it has been shown both experimentally and numerically that the density of adsorbed particles on a charged pattern grows as \sqrt{t} at long times. A simple two-step transport model, in excellent agreement with simulations and consistent with experiments, reveals that this behavior is due to a diffusive limitation of mass transfer in the bulk of the suspension. It is important to note that “diffusion” includes here thermal agitation and colloid–colloid repulsive interactions, the latter dominating the former by far. In conclusion, increasing the number of particles assembled on charged patterns requires increasing colloid–colloid repulsions, which can be achieved by increasing the colloidal concentration, the colloidal surface charge, or the screening length. Increasing the pattern charge amplitude is not critical because it is already large enough for the charged pattern–colloid interactions to be nonlimiting. In brief, as far as physico-chemical levers are concerned, nanoxerography works more efficiently by increasing the osmotic pressure of the colloidal suspension. If this is not an option, as in the present experimental system, we show in the next part that hydrodynamics can be introduced to enhance the performances of nanoxerography.

Assembly Mechanisms in Convective Nanoxerography Applied to $1 \mu\text{m}$ Particles. In order to increase the density of particles assembled on charged patterns, we

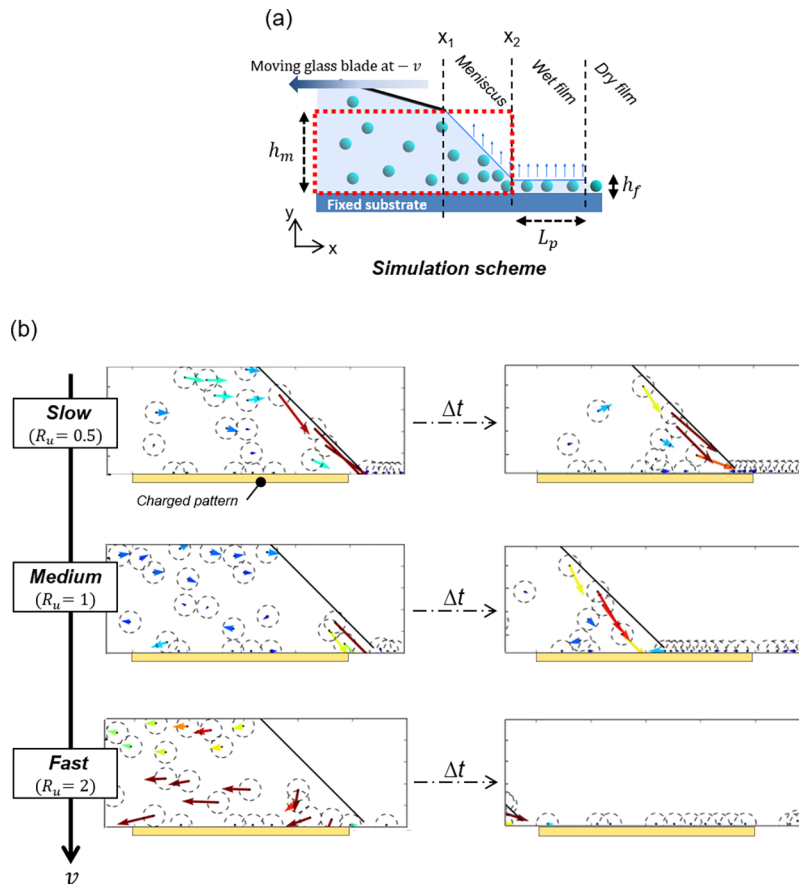


Figure 3. (a) Scheme of the idealized configuration used for the convective development simulations with the red rectangle defining the simulation domain and (b) snapshots of the displacements of $1 \mu\text{m}$ latex particles in these simulations. The arrows represent the instantaneous velocity vectors with a length proportional to the velocity magnitude. The dimensionless parameter R_u is defined as the ratio $\frac{|u_m|}{|u_e|}$.

introduced the effect of an evaporation-induced flow field. This so-called “convective nanoxerography process” (Scheme 1) is inspired from the convective self-assembly (CSA)²⁵ technique which rests on the formation of an evaporation-induced flow of solvent from the bulk of the drop to the triple line defined as the air/solvent/substrate meniscus interface. This flow transports particles toward and inside the meniscus, and finally brings them to the substrate surface to form different coating-like films^{26,27} or lines.²⁸ In these experiments, as in the simulations described hereafter, the substrate was dragged under the blade immediately after the drop was deposited so the static contact time t_{sc} is close to zero and the full assembly process is influenced by hydrodynamics. The diffusive regime described in the previous part is thus absent, which facilitates the analysis of the influence of hydrodynamics. Note however that for practical applications, more particles can be adsorbed on the charged patterns if a non-zero static contact time is allowed before dragging the blade.

Optical microscopy recordings reveal that the first particles rapidly adsorbed on the charged substrate act as anchoring sites for the triple line. The interface of the drop then takes the form depicted in Figure 3a with a meniscus followed by a wet film of height $h_f \simeq d$ and of length $L_p \approx 1 \text{ mm}$.

Numerical simulations were performed to evaluate the $1 \mu\text{m}$ particle motion qualitatively during a convective nanoxerography process and to analyze the capabilities offered by the convective phenomenon. The geometric configuration was slightly different from the experimental one for the sake of

simplicity (Figure 3a). The numerical domain was restricted to $y < h_m$, where h_m is the height of the glass blade tip, so the blade was not explicitly included. The particle dynamics were computed in the substrate reference frame as before, with the additional effect of a model background flow field $\mathbf{u} = \mathbf{u}_m + \mathbf{u}_e$.

The mostly uniform flow $\mathbf{u}_m \approx (-v, 0)$ is due to the blade-induced motion of the meniscus only (without evaporation) and \mathbf{u}_e is the evaporation-induced flow under the blade that would exist even with fixed glass blade and substrate. Hydrodynamic interactions between particles can be neglected in the present dilute regime.

Particles located in the wet film ($x > x_2$) (see Figure 3a) are considered trapped so \mathbf{u} only needs to be computed for $x < x_2$. In the wet layer, particles are quite distant and the layer height $h_f \approx d$ is much smaller than its length L_p so $\mathbf{u}_e(x_2, y)$ can be estimated using the Navier–Stokes equation with the lubrication approximation (gradients along the film are much smaller than in the direction perpendicular to the substrate), a no-slip condition on the substrate, and a slip condition at the free surface.

$$\frac{\partial p}{\partial x} = \eta \frac{\partial^2 u_e}{\partial x^2} \quad (5)$$

$$\frac{\partial p}{\partial y} = 0 \quad (6)$$

$$\left. \frac{\partial u}{\partial y} \right|_{y=h_f} = 0; \quad u(0) = 0 \quad (7)$$

The solution is

$$\mathbf{u}_e(x_2, y) = \begin{bmatrix} -\frac{3Q_e}{2h_f^3}y(y-2h_f) \\ 0 \end{bmatrix} \quad (8)$$

where $Q_e = v_e L_p$ is the total evaporation-induced flow rate per unit length of the drying film at position x_2 and v_e is the evaporation rate depending only on thermodynamics. The wet layer length L_p is imposed by a balance between the capillary pressure at the end of the wet film and the pressure loss due to viscous dissipation in the film,²⁹ and is of the order of 1 mm.

There is no clear boundary condition at $y = h_m$ below the blade ($x < x_1$) so for simplicity the same form of flow field is used with h_f replaced by the blade height h_m . Note that in doing so the flux evaporated along the meniscus is neglected.

Finally, below the meniscus joining the glass blade and the one-particle layer ($x_1 \leq x \leq x_2$), the lubrication approximation is questionable. The form of the previous equation will however be retained to produce an analytical approximation of the flow field. The height h_f is replaced by the local meniscus height $h(x) = h_m + x_1 - x$ (the meniscus is assumed to be flat and inclined at 45°). The vertical velocity is found by solving the continuity equation $\nabla \cdot \mathbf{u}_e = 0$ and the result is

$$\mathbf{u}_e(x_1 \leq x \leq x_2, y) = -\frac{3Q_e}{2h(x)^3}y(y-2h(x)) \begin{bmatrix} 1 \\ -\frac{y}{h(x)} \end{bmatrix} \quad (9)$$

This imposed flow is only a model but it imposes the correct total flow rate Q_e and it respects mass conservation. The main goal of these simulations is to illustrate the competition between the evaporation-induced flow \mathbf{u}_e driving particles toward the substrate and the blade/meniscus-induced flow \mathbf{u}_m swiping particles toward the left without helping deposition. Note that the simulation methodology used here, with its approximate treatment of hydrodynamics, is indeed sufficient to draw these conclusions. However, obtaining more quantitative data would require a refinement of the numerical method beyond what exists presently (solve the flow between particles and possibly in the gas phase, include solvent properties jump at the free surface for electrostatics, include triple-line calculation for the dewetting process...).

Simulation results are schematically shown in Figure 3b as a function of the dragging speed and the corresponding numerical simulations videos are available in Supporting Information. For

low dragging speeds ($R_u \equiv \frac{|u_m|}{|u_e|} < 1$), the simulation snapshots displayed in Figure 3b show that the particle velocity vectors are mainly pointing toward the meniscus and the substrate. This is because the hydrodynamic flow is mainly induced by evaporation in the thin wet film and is therefore convergent toward the substrate. Particles that were unable to reach the substrate by diffusion alone on the experimental time scale are brought in its vicinity by convection. The latter thus contributes to bring more particles in the electrostatic attraction range of charged patterns and so increases the density of particles per pattern, but also out of charged patterns as shown in Figure 3b. The convective flow is considered as “constructive” in this case.

For large dragging speeds ($R_u > 1$), the evaporation-induced flow is negligible compared to the swiping flow due to the displacement of the blade and meniscus and particles are mainly translated laterally above the charged patterns as illustrated by the snapshot shown in Figure 3b. In this case, the weak evaporation-induced flow is useless. Simulations reveal that particles are deposited mainly on the charged patterns, although not very densely, so the nanoxerography process remains selective. When the blade-induced and the evaporation-induced flows are of comparable amplitudes ($R_u \simeq 1$), a rotating motion can be observed under the meniscus (see snapshot in Figure 3b and numerical videos in Supporting Information). It is generated by the local dominance of \mathbf{u}_e or \mathbf{u}_m for different altitudes y over the substrate. In this regime, particles are deposited both on and out of charged patterns, but the assembly is significantly denser on the charged patterns.

In these simulations, it can be observed that the convective flow contribution is actually efficient beyond classical electrostatic contribution only when R_u is smaller than about 1. However, at the same time, if this ratio is too small, simulations reveal a more uniform deposition similar to what is obtained in classical CSA and the interesting selectivity of nanoxerography is lost.

So far, simulations have shown that the enhancement of assembly by convection is characterized by the dimensionless parameter $R_u \equiv \frac{|u_m|}{|u_e|}$. As these simulations remain qualitative because of the use of an idealized flow field, $1 \mu\text{m}$ latex particle assemblies were also carried out by convective nanoxerography at different dragging speeds v ranging from 5 to $80 \mu\text{m}\cdot\text{s}^{-1}$, with $t_{sc} = 0$ to isolate the effect of v . Results are presented on Figure 4.

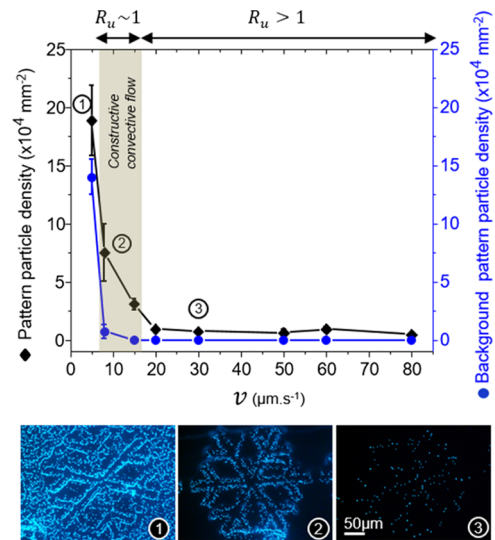


Figure 4. Pattern and background particle densities for $\rho_b = 6.825 \times 10^8 \text{ mL}^{-1}$ as a function of the dragging speed with fluorescent optical microscopy images of corresponding assemblies, (b) example of $4.3 \mu\text{m}$ particle assemblies obtained with optimized parameters using convective nanoxerography

The observation that $\rho_p > \rho_{bg}$ for the full v range confirms that charged patterns still act as selective electrostatic traps forming monolayered particle assemblies, even with the existence of the evaporation-induced flow. Both pattern and background densities reach a plateau regime characterized by very low particle capture for speeds larger than $15\text{--}20 \mu\text{m}\cdot\text{s}^{-1}$ (region 3 in

Figure 4). From the measured average evaporation rate of IPA in still air and the geometry of the meniscus, we estimated $u_e \approx 12 \mu\text{m/s}$ in these experiments, so this plateau regime corresponds to the $R_u > 1$ case identified in simulations. Below this threshold, ρ_p and ρ_{bg} both increase with decreasing dragging speed, also as expected from simulations. The former increases faster than the latter, indicating a good selectivity of the assembly, for $v > 5 \mu\text{m}\cdot\text{s}^{-1}$ (region 2 in Figure 4). Finally, for too low dragging speeds (region 1 in Figure 4), the evaporation-induced flow predominance can lead to the deposition of particles outside charged patterns in a way similar to the usual CSA process. In the present example, the case $v = 8 \mu\text{m}\cdot\text{s}^{-1}$ represents the best compromise because selectivity is preserved, the assembly time is reduced by 40% compared to conventional nanoxerography (when the latter works). The experimental observations and the simulation results described above are thus perfectly consistent with each other.

We have demonstrated that, when coupled to nanoxerography, convective effects increase the particle deposition rate for low enough blade velocities, but also decrease the selectivity of the assembly. Convective nanoxerography is thus an efficient technique to assemble micrometer-sized particles for a range of blade velocities depending on the setup geometry, dispersion density, and evaporation rate. Analyses of the effects of the latter two parameters are reported in detail in Supporting Information (Figures S6 and S7). In short, both the pattern and the background densities increase with the particle concentration of colloidal dispersion experimentally which is confirmed by simulations. Simulations also demonstrated that the effective diffusion coefficient D increased with concentration. Finally, a working concentration of $\rho_b = 6.825 \times 10^8 \text{ mL}^{-1}$ gives a pattern particle density high enough ($\rho_p > 5 \times 10^4 \text{ mm}^{-2}$) with a good selectivity ($S > 0.8$). On another hand, the solvent evaporation rate directly increases with the substrate temperature and makes the convective flow speed up, which increases the particle flux toward the triple line. In addition, the viscosity of the solvent heated by the substrate diminishes by about 30%, and the particle diffusion coefficient D_0 increases by about 30%. Both phenomena facilitate particle displacements to the edge of the meniscus. A working temperature just below 20°C prevents the predominance of convective flow effects and allows the analysis of other parameters.

Figure 5 presents an example of directed assembly of $1 \mu\text{m}$ latex particles on a large scale using the optimized parameters determined above. It proves that the proposed assembly process is robust, reproducible, and scalable.

Assembly Mechanisms in Convective Nanoxerography Applied to Larger 4.3 and $10 \mu\text{m}$ Particles. Experiments were also extended for different sizes of latex

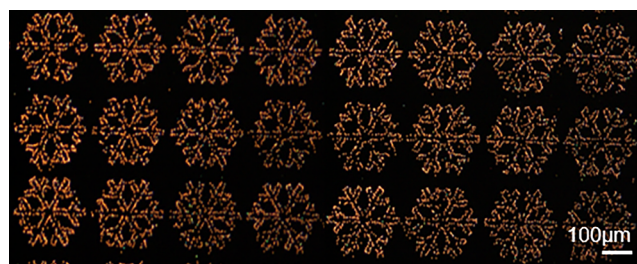


Figure 5. Example of $1 \mu\text{m}$ particle assembly obtained with optimized parameters ($\rho_b = 6.825 \times 10^8 \text{ mL}^{-1}$, $T = 20^\circ\text{C}$, $t_{sc} = 120 \text{ s}$, $v = 40 \mu\text{m}\cdot\text{s}^{-1}$) using convective nanoxerography.

particles (500 nm , $4.3 \mu\text{m}$, and $10 \mu\text{m}$). Results reported in Supporting Information (Figure S8) confirmed that the presented technique is efficient to selectively assemble the ones with a diameter smaller than $10 \mu\text{m}$. Kinetics of 500 nm particles were similar to the ones described for $1 \mu\text{m}$ spheres and showed that around this particle size range, conventional nanoxerography starts to face troubles in making particle assemblies. Dense and selective assemblies of $4.3 \mu\text{m}$ latex particles were made, thanks to the convective nanoxerography process using optimized parameters similar to the previous ones found for $1 \mu\text{m}$ particles (Movie M1). However, their assembly kinetics varied from $1 \mu\text{m}$ particles. Indeed, a “constructive” sedimentation phenomenon contributed to the particle displacement toward the charged patterns ($v_{sed}(4.3 \mu\text{m}) = 1.31 \mu\text{m}\cdot\text{s}^{-1}$, whereas $v_{sed}(1 \mu\text{m}) = 0.071 \mu\text{m}\cdot\text{s}^{-1}$)³⁰ and was superimposed to the “constructive convective flow” found in $1 \mu\text{m}$ particle assembly kinetics. $10 \mu\text{m}$ particle assemblies were also obtained but it seems to be the upper size limit in the case of our experiments because the effect of sedimentation became predominant along with a large increase of capillary and hydrodynamic forces which tended to decrease selectivity. Such issues might be partially solved by enlarging the dimensions of the charged pattern and upgrading the experimental set up to gain a finer control over solvent evaporation, but particle–substrate attractions will eventually be overcome by the shear-flow induced by the blade displacement for too large particles.

■ CONCLUSIONS

This work aimed to elucidate and overcome the limitation of nanoxerography (i.e., the electrostatic directed assembly of particles on charged patterns on a substrate) for micrometer-sized particles. Numerical simulations and experiments of conventional nanoxerography revealed its two major limits, (i) the need of a well-controlled triple line motion during drying to avoid heterogeneous dewetting, and (ii) the need of a long contact time and of a high osmotic pressure of the colloidal suspension to allow bringing particles in the electrostatic attraction range of charged patterns by collective diffusion. We proposed to couple a blade coating technique to nanoxerography, which immediately solves the first problem and introduces a solvent evaporation-induced flow bringing particles near the substrate faster than diffusion to remove the second bottleneck. This new “convective nanoxerography” process thus paves the way of new possibilities for the directed assembly of large particles, expanding by a factor 40 at least the size range foreseeable.

■ ASSOCIATED CONTENT

📄 Supporting Information

The Supporting Information is available free of charge on the ACS Publications website at DOI: [10.1021/acs.jpcc.8b08981](https://doi.org/10.1021/acs.jpcc.8b08981).

All the details, extra experiments, and numerical simulations used in this work, full list of used materials, description of the electrical microcontact technique and the convective nanoxerography set up upgraded in this work, assembly results of $1 \mu\text{m}$ latex particles in conventional nanoxerography, the analysis program employed on optical images for particles counting, the modeling of particle–substrate interaction and the determination of the electrostatic boundary condition, calculations of the collective diffusion and the influence of the static contact time and dragging speed, and assembly

experiments on the influence of the substrate temperature, concentration, and size of particles (PDF)

Simulation video 1: $R_u = 0.5$ case (MPG)

Simulation video 2: $R_u = 1$ case (MPG)

Simulation video 3: $R_u = 2$ case (MPG)

M1 movie: convective nanoxerography applied to 1 μm particles (MPG)

AUTHOR INFORMATION

Corresponding Author

*E-mail: laurence.ressier@insa-toulouse.fr. Phone: +33(0)5 61 55 96 72.

ORCID

Yannick Hallez: 0000-0001-5172-439X

Etienne Palleau: 0000-0002-9923-4936

Laurence Ressier: 0000-0003-1343-0117

Notes

The authors declare no competing financial interest.

ACKNOWLEDGMENTS

This work was performed using HPC resources from GENCI-CINES/IDRIS (grant A0040910109) and CALMIP (grant P17001).

REFERENCES

- (1) Zhang, L.; Zhu, Y. Directed Assembly of Janus Particles under High Frequency Ac-Electric Fields: Effects of Medium Conductivity and Colloidal Surface Chemistry. *Langmuir* **2012**, *28*, 13201–13207.
- (2) Flauraud, V.; Mastrangeli, M.; Bernasconi, G. D.; Butet, J.; Alexander, D. T. L.; Shahrabi, E.; Martin, O. J. F.; Brugger, J. Nanoscale Topographical Control of Capillary Assembly of Nanoparticles. *Nat. Nanotechnol.* **2016**, *12*, 73–80.
- (3) Ginger, D. S.; Zhang, H.; Mirkin, C. A. The Evolution of Dip-Pen Nanolithography. *Angew. Chem., Int. Ed.* **2004**, *116*, 30–46.
- (4) Stelling, C.; Mark, A.; Papastavrou, G.; Retsch, M. Showing Particles Their Place: Deterministic Colloid Immobilization by Gold Nanomeshes. *Nanoscale* **2016**, *8*, 14556–14564.
- (5) Vogel, N.; Retsch, M.; Fustin, C.-A.; del Campo, A.; Jonas, U. Advances in Colloidal Assembly: The Design of Structure and Hierarchy in Two and Three Dimensions. *Chem. Rev.* **2015**, *115*, 6265–6311.
- (6) Grzelczak, M.; Vermant, J.; Furst, E. M.; Liz-Marzán, L. M. Directed Self-Assembly of Nanoparticles. *ACS Nano* **2010**, *4*, 3591–3605.
- (7) Sangeetha, N. M.; Moutet, P.; Lagarde, D.; Sallen, G.; Urbaszek, B.; Marie, X.; Viau, G.; Ressier, L. 3D Assembly of Upconverting NaYF₄ Nanocrystals by AFM Nanoxerography: Creation of Anti-Counterfeiting Microtags. *Nanoscale* **2013**, *5*, 9587.
- (8) Tzeng, S.-D.; Lin, K.-J.; Hu, J.-C.; Chen, L.-J.; Gwo, S. Templated Self-Assembly of Colloidal Nanoparticles Controlled by Electrostatic Nanopatterning on a Si₃N₄/SiO₂/Si Electret. *Adv. Mater.* **2006**, *18*, 1147–1151.
- (9) Mesquida, P.; Stemmer, A. Attaching Silica Nanoparticles from Suspension onto Surface Charge Patterns Generated by a Conductive Atomic Force Microscope Tip. *Adv. Mater.* **2001**, *13*, 1395–1398.
- (10) Seemann, L.; Stemmer, A.; Naujoks, N. Local Surface Charges Direct the Deposition of Carbon Nanotubes and Fullerenes into Nanoscale Patterns. *Nano Lett.* **2007**, *7*, 3007–3012.
- (11) Moutet, P.; Sangeetha, N. M.; Ressier, L.; Vilar-Vidal, N.; Comesaña-Hermo, M.; Ravaine, S.; Vallée, R. A. L.; Gabudean, A. M.; Astilean, S.; Farcau, C. Surface-Enhanced Spectroscopy on Plasmonic Oligomers Assembled by AFM Nanoxerography. *Nanoscale* **2015**, *7*, 2009–2022.

(12) Teulon, L.; Palleau, E.; Morales, D.; Poirot, D.; Ressier, L. Interactive Nanogel Marking at the Microscale for Security and Traceability Applications. *Adv. Mater. Technol.* **2017**, *3*, 1700244.

(13) Morales, D.; Teulon, L.; Palleau, E.; Alnasser, T.; Ressier, L. Single-Step Binary Electrostatic Directed Assembly of Active Nanogels for Smart Concentration-Dependent Encryption. *Langmuir* **2018**, *34*, 1557–1563.

(14) Moutet, P.; Lacroix, L.-M.; Robert, A.; Impéror-Clerc, M.; Viau, G.; Ressier, L. Directed Assembly of Single Colloidal Gold Nanowires by AFM Nanoxerography. *Langmuir* **2015**, *31*, 4106–4112.

(15) Fudouzi, H.; Kobayashi, M.; Shinya, N. Site-Controlled Deposition of Microsized Particles Using an Electrostatic Assembly. *Adv. Mater.* **2002**, *14*, 1649–1652.

(16) Barry, C. R.; Steward, M. G.; Lwin, N. Z.; Jacobs, H. O. Printing Nanoparticles from the Liquid and Gas Phases Using Nanoxerography. *Nanotechnology* **2003**, *14*, 1057–1063.

(17) Jacobs, H. O.; Whitesides, G. M. Submicrometer Patterning of Charge in Thin-Film Electrets. *Science* **2001**, *291*, 1763–1766.

(18) Sessler, G. M. Electrets: Recent Developments. *J. Electrostat.* **2001**, *51*–52, 137–145.

(19) Palleau, E.; Sangeetha, N. M.; Viau, G.; Marty, J.-D.; Ressier, L. Coulomb Force Directed Single and Binary Assembly of Nanoparticles from Aqueous Dispersions by AFM Nanoxerography. *ACS Nano* **2011**, *5*, 4228–4235.

(20) Hallez, Y.; Diatta, J.; Meireles, M. Quantitative Assessment of the Accuracy of the Poisson–Boltzmann Cell Model for Salty Suspensions. *Langmuir* **2014**, *30*, 6721–6729.

(21) Hallez, Y.; Meireles, M. Modeling the Electrostatics of Hollow Shell Suspensions: Ion Distribution, Pair Interactions, and Many-Body Effects. *Langmuir* **2016**, *32*, 10430–10444.

(22) Hallett, J. E.; Gillespie, D. A. J.; Richardson, R. M.; Bartlett, P. Charge Regulation of Nonpolar Colloids. *Soft Matter* **2018**, *14*, 331–343.

(23) Russel, W. B.; Saville, D. A.; Schowalter, W. R. *Colloidal Dispersions*; Cambridge University Press, 1989.

(24) Bell, G. M.; Levine, S.; McCartney, L. N. Approximate Methods of Determining the Double-Layer Free Energy of Interaction between Two Charged Colloidal Spheres. *J. Colloid Interface Sci.* **1970**, *33*, 335–359.

(25) Malaquin, L.; Kraus, T.; Schmid, H.; Delamar, E.; Wolf, H. Controlled Particle Placement through Convective and Capillary Assembly. *Langmuir* **2007**, *23*, 11513–11521.

(26) Jiang, C.; Li, L.; Pong, P. W. T. Controlled Convective Self-Assembly of Silver Nanoparticles in Volatile Organic Solvent and Its Application in Electronics. *RSC Adv.* **2015**, *5*, 98747–98756.

(27) Dimitrov, A. S.; Nagayama, K. Continuous Convective Self-Assembly of Fine Particles into Two-Dimensional Arrays on Solid Surfaces. *Langmuir* **1996**, *12*, 1303–1311.

(28) Farcau, C.; Moreira, H.; Viallet, B.; Grisolia, J.; Ressier, L. Tunable Conductive Nanoparticle Wire Arrays Fabricated by Convective Self-Assembly on Nonpatterned Substrates. *ACS Nano* **2010**, *4*, 7275–7282.

(29) Goehring, L.; Clegg, W. J.; Routh, A. F. Solidification and Ordering during Directional Drying of a Colloidal Dispersion. *Langmuir* **2010**, *26*, 9269–9275.

(30) Meglio, J.-M. D. *Colloïdes et Nanosciences in Techniques de l'Ingénieur*, 2007; p 19.

Supporting information

Electrostatic Directed Assembly of Colloidal Microparticles Assisted by Convective Flow

*Lauryanne Teulon¹, Yannick Hallez², Simon Raffy¹, François Guerin¹, Etienne Palleau¹ and
Laurence Ressier^{1,*}*

¹LPCNO, Université de Toulouse, CNRS, INSA, UPS, 135 Avenue de Rangueil, 31077
Toulouse, France

²Laboratoire de Génie Chimique, Université de Toulouse, CNRS, INPT, UPS, Toulouse,
France

* Author to whom correspondence should be addressed: laurence.ressier@insa-toulouse.fr /
+33(0)5.61.55.96.72

Materials

Colloidal dispersions of fluorescent carboxylate latex particles with five different diameters (100 nm, 500 nm, 1 μm , 4.3 μm and 10 μm) were purchased from PolyScience[®] (Fluoresbrite[®] YG Carboxylate Microspheres, $\lambda_{em} \approx 486$ nm). These negatively charged particles were chosen as model ones for this study because they exist in a same size assortment and their fluorescence helps their characterization by optical microscopy. Prior to use, all solutions were centrifuged at 15000 rpm during 30min in water to remove excess ligands. Isopropanol (IPA, 99.5%) was then used to dilute particle dispersions for all experiments.

Electrical microcontact printing (e- μ CP)

The first step of the nanoxerography protocol was performed by electrical microcontact printing method (e- μ CP) on 100 nm PolyMethylMethAcrylate thin films spin-coated on highly doped silicon wafers. A magnetic and electrically conductive PolyDiMethySiloxane stamp featuring patterns of desired geometries was used. Following a previously described protocol¹ based on a modified Innostamp 40 equipment, a magnetic pressure was applied owing to a matrix of magnets carefully positioned under the substrate. It allowed to ensure a homogeneous and reproducible contact between the PMMA thin film and the patterned stamp even on large surfaces up to a 4 inch wafer.² A DC voltage of 40V was applied between the conductive PDMS stamp and the substrate during 45s. It resulted in the creation of multiple positively charged snowflakes patterns with a 250 μm width. The choice of such micrometer wide patterns facilitates the in-situ optical observations and characterization of large latex particles assemblies, while showing complex details on their branches.

1 μm latex particles assembly by conventional nanoxerography using immersion development

Conventional nanoxerography protocol including a manual immersion of a charged sample in a colloidal bath followed by manual withdrawal was used to assemble negatively charged 1 μm latex particles. A fixed colloidal dispersion concentration of $\rho_0 = 6.825 \times 10^8 \text{ mL}^{-1}$ was used while varying t_{sc} between 30s and 5min.

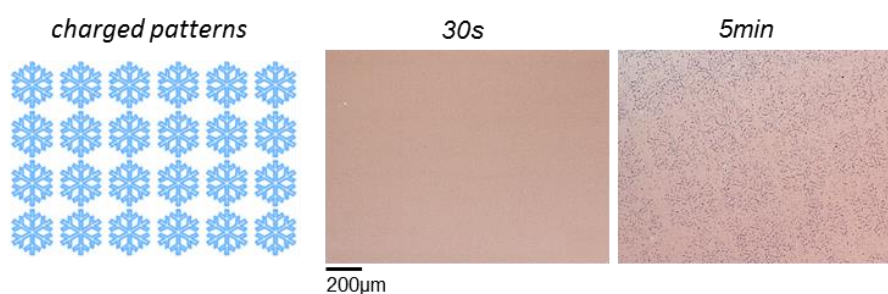


Figure S1. Image of the expected charged patterns given for sake of clarity (left). Optical microscopy image of 1 μm particle assemblies made with nanoxerography using a static contact time of either 30s (middle) or 5min (right).

No particle assembly was observed for $t_{sc} = 30\text{s}$ while some particle assembly, with poor density and selectivity, was obtained for $t_{sc} = 300\text{s}$ and a slow manual withdrawal of the substrate. These experiments also reveal that the way the solvent evaporates during t_{dc} strongly affects the particle assembly. A natural (non-controlled) evaporation of the solvent indeed leads to a seemingly random dewetting of the substrate and to the creation of several dispersion droplets. Evaporation of the latter generates particle aggregates at locations independent of the presence of charged patterns.

Convective nanoxerography set up

A homemade CSA deposition system was used to drag a drop of colloidal dispersion using a glass blade inclined at an angle of 20° at 200-300 μm above the horizontal substrate fixed to a temperature-regulated copper plate (see **Scheme 1** of the paper). Temperature regulation was controlled from 17°C to 25°C . A 10-15 μL particle dispersion drop was injected between the blade and the substrate. The meniscus formed by the colloidal dispersion over the substrate was put in translational motion by dragging the stage under the substrate at dragging speeds ranging from 5 to 100 $\mu\text{m}\cdot\text{s}^{-1}$. All experiments were performed in ambient air, at room

temperature (20°C), and a relative humidity RH 40%. The setup was mounted under an optical microscope to allow real-time observations.

A syringe pump system was used to balance the solvent evaporation during the static contact time analysis. First, the 10-15 μL drop of the particle dispersion was deposited between the glass blade and the charged substrate. Then the syringe pump system was used to have a continuous supply of solvent (IPA). The whole system was set to locate the needle below the glass slide at the back of the dispersion drop. An IPA flow rate of 1.11 $\mu\text{L}/\text{min}$ was fixed thanks to empirical determination of the pure solvent evaporation rate. The pumping system was turned on during the whole static contact period of time, the needle was removed at the end of it and the stage was translated to go on the convective flow development with parameters depending on the final aim.

Matlab image analysis program

To determine the particle density on a snowflake pattern while assembling 1 μm latex particles, a homemade Matlab[®] program was used to analyze fluorescent optical microscopy images. From these optical images, four particle based snowflake patterns were observed by sample to evaluate the reproducibility of the process.

The pictures used in the analysis program were taken by a microscope under fluorescent conditions equipped with a 20x (while observing particles on patterns) and 50x (while observing particles out of patterns) magnification. To start the analysis, the blue matrix of the RGB 8 bits microscopic picture (0 to 255) is extracted. To select the particles on the snowflake pattern, the blue image is multiplied by a logical image L1 of the snowflake pattern: the value 1 if on, and 0 if out of patterns: everything out of the pattern is consequently considered to be zero. A logical condition is applied to the image with a threshold T1 fixed at a level corresponding to half the maximum level of the image in order to separate particles and particle clusters from the background. A new small matrix is created for each separated object (single particles or particle clusters). All these small matrices are then multiplied by the corresponding part of the blue matrix (**Figures S2.a-b**).

For each small matrix, an iteration is used from the level corresponding to half of the maximum level of the blue matrix up to the maximum one. Each iteration value leads to a threshold T2 to get various logical images. The average coordinates x and y are calculated from all 1 values of

all logical images. With those data, statistical centers or centroids of the objects/particles are obtained (see red cross on Figure S2a&b). A profile is created with the blue matrix levels as a function of the length of each pixel to these centroids (**Figures S2.c-d**).

After the analysis treatment, a single particle has a near-Gaussian profile (see **Figure S2.c**) while other objects (two particles or more) have hysteresis like profiles (see **Figure S2.d**). By derivating such profiles, single particles from multiple ones are separated.

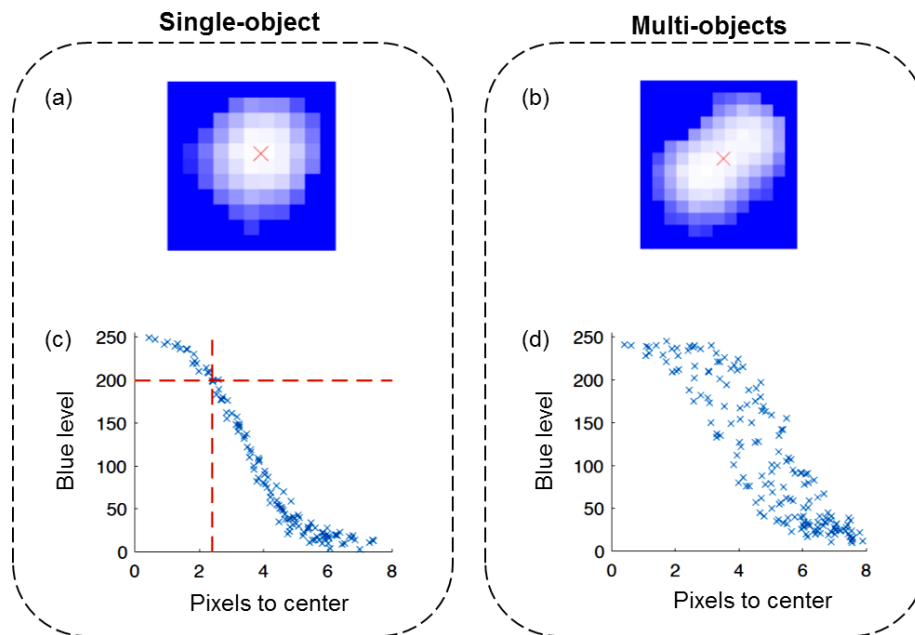


Figure S2. Image analysis for (a,c) single object (b,d) multi-objects. (a,b) Numerical images created for the analysis. The red crosses are the positions of the calculated centers. The solid blue is the threshold (where logical images = 0). The interne color variations are the corresponding part of the blue matrix. (c,d) Profiles of the particles: blue level as a function of the length of each pixel to the center.

The comparison of the real radius of one particle (converted in pixels) with a single particle profile gives a specific blue level, further used as a threshold T3. This comparison is done for each single particle detected on the full image.

The average value of all T3 thresholds gives a threshold T4 applied on each object (single or multiple particles) to shape them to their physical dimensions converted to specific pixel areas. These pixel areas are divided by the real physical cross-section of a particle (converted in pixels²) to get a normalized number of particles for each object (*Nb*).

Due to the fluorescent overlapping when considering particle clusters, the image treatment detailed above results in the addition of extra pixels (an extra artefact surface S) at the interfaces between particles that virtually increase the number of pixels in the case of complex objects

(two or more particle based clusters). To find the correct number of particles (Nb_{cor}), a logistic map is applied to all Nb (equation 1).

$$Nb_{cor} = Nb - 2 * \alpha * (Nb - 1) \quad (1)$$

Where α is the corrective factor (between 0 and 0.2) corresponding to S . α is adjusted to get the best fit with the integer number of particles by objects (**Figure S3**).

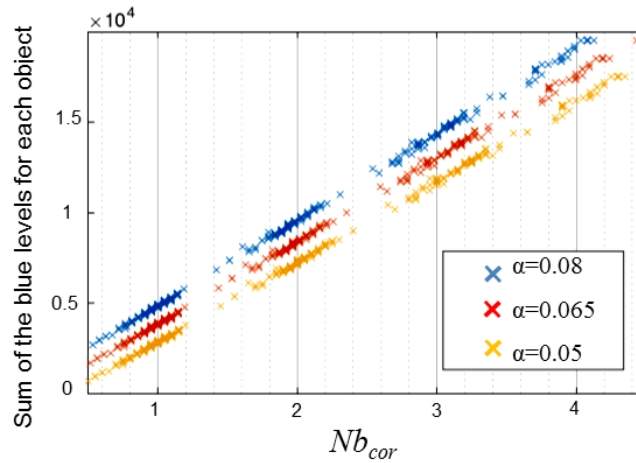


Figure S3. Sum of the blue levels of each object as function of Nb_{cor} in the case of an assembly of $1 \mu\text{m}$ particles (dragging speed $8\mu\text{m}\cdot\text{s}^{-1}$, $t_{ic} = 275\text{s}$, concentration = $3\rho_0/2$). Blue and yellow set of points have respectively an ordinate offset $+10^3$ and -10^3 for sake of clarity.

The number of particles on each snowflake pattern is given by the sum ΣNb_{cor} . The Nb_{cor} for $\alpha = 0,065$ gives the best fit for the objects from 1 to 4 particles (**Figure S3**).

It is worth noting that, since α is manually defined, it induces some errors that have to be taken into account. These errors calculated for all images, vary from 1 to 9%.

The sum of all pixels of a logical image L1 gives a pattern area with pixel^2 as unit. To get the final particle density, the number of particles is divided by the surface of the corresponding snowflake pattern. With the magnitude of the microscope, the unit is converted from $\text{particle}/\text{pixel}^2$ to $\text{particle}/\text{mm}^2$.

Determination of the electrostatic boundary condition on 1 μ m latex particles in isopropanol

The electrophoretic mobility of 1 μ m latex particles in isopropanol was measured with a Zeta Potential Particle Analyzer (Beckman Coulter) for a wide range of particle volume fraction $10^{-5} < \phi < 10^{-2}$ (**Figure S4**). Data were an average of 5 measurements with 30s acquisition times. The samples were allowed to equilibrate thermally at the desired temperature for 5min before the measurements. Electrophoretic mobility was calculated using the Laser Doppler Method. In this system, the mobility decreases with volume fraction even in relatively dilute conditions due to the presence of long-range interactions. This behavior is dependent on the balance between hydrodynamic and electrostatic forces, the latter depending on the electrostatic boundary condition (BC) on the surface of particles. These BC can thus be deduced from the fitting of experimental data with an adequate model. Here we used an expression developed by Ohshima with a cell model.³ This expression, valid in the context of the linearized Debye Hückel theory for electrostatics, reads

$$\mu = \frac{2\epsilon\zeta}{3\eta} \int_a^b H(r) \left(1 + \frac{a^3}{2r^3}\right) dr + \frac{2\epsilon(\kappa a)^2}{9\eta(1-\phi)} \psi^{(0)}(b) \left(1 + \frac{a^3}{2b^3}\right) \left(1 + \frac{b^3}{a^3} - \frac{9b^2}{5a^2} - \frac{a^3}{5b^3}\right),$$

where

$$H(r) = -\frac{(\kappa a)^2}{6\zeta(1-\phi)} \left[1 - \frac{3r^2}{a^2} + \frac{2r^3}{a^3} - \frac{a^3}{b^3} \left(\frac{2}{5} - \frac{r^3}{a^3} + \frac{3r^5}{5a^5} \right) \right] \frac{d\psi^0}{dr} \quad (2)$$

and a is the particle radius, $b = a\phi^{-\frac{1}{3}}$ is the radius of the cell, ϵ is the solvent dielectric constant and η its dynamic viscosity, ζ is the particle effective surface potential, κ^{-1} is the effective screening length, and $\psi^{(0)}$ is the (unscaled) electrostatic potential field in the cell model. This expression has then been fitted to the experimental mobility data by adjusting κ and ζ . The consistence between theoretical and experimental data for constant values of these parameters ($\kappa a = 0.05$ and $\zeta = 0.086$ V) indicate that a constant effective surface potential is pertinent for the present experimental system. This kind of behavior has already been reported in literature for functionalized PMMA/PHSA particles dispersed in dodecane and corresponds to a charge regulation mechanism (see ⁴ and references therein). Interestingly, the range of electrostatic interactions is measured to be of the order of 10 μ m in the present system, which corresponds to 10 particle diameters. This explains why the particle collective diffusion coefficient is very large compared to the Stokes-Einstein value even in what would seem dilute conditions (volume fraction less than 0.26%).

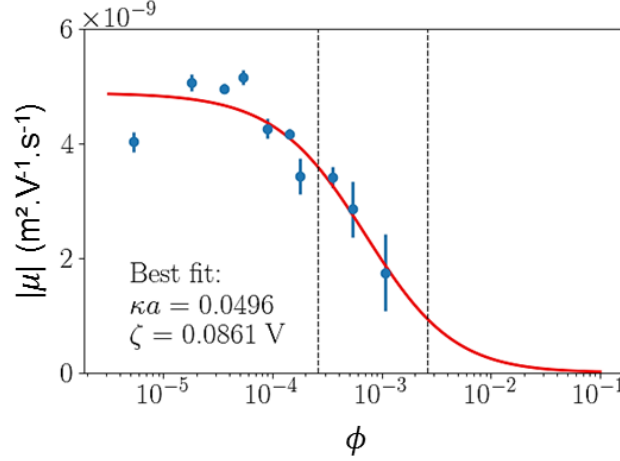


Figure S4. Electrophoretic mobility variation as a function of the volume fraction for 1 μ m latex particles. Experimental data: blue symbols; Model: red curve. The vertical dashed lines indicate the range of volume fractions corresponding to the range of bulk particle concentrations C_b investigated in the article ($C_0/5 < C_b < 2C_0$).

Particle-substrate electrostatic force modelling

A model for the particle-substrate electrostatic force is required to solve the transport equation in the first regime. This regime corresponds to the capture of particles above the substrate at a distance smaller than about one or two Debye lengths. Unfortunately, classical DLVO-type force models are in principle valid for separation distances larger than that. To determine which model can be used in the transport equation, we performed full 3D Debye-Hückel simulations of one particle above a charged plate and measured the interaction force for the physico-chemical conditions used in the many-body simulations. The results are reported in **Fig. S5** as a function of the separation distance y scaled by the Debye length. The linear superposition approximation (LSA)⁴

$$F_{LSA} = -\epsilon \left(\frac{kT}{e} \right)^2 4\pi\kappa a \psi_s \psi_p e^{-\kappa(y-a)} \quad (3)$$

underestimates the interaction force for all the distances investigated. This was expected as this is a result derived in the limit of weakly overlapping double layers. The Hogg, Healy & Fuerstenau (HHF) approximation⁵

$$F_{HHF} = -\epsilon \left(\frac{kT}{e} \right)^2 2\pi \kappa a \frac{2\psi_s \psi_p e^{-\kappa(y-a)} - (\psi_s^2 + \psi_p^2) e^{-2\kappa(y-a)}}{1 - e^{-2\kappa(y-a)}} \quad (4)$$

is in better agreement with simulations. It recovers numerical results perfectly as soon as $\kappa y > 1$. Solving the transport equation with this full equation is however difficult. In order to have a tractable equation, we used the force model $F = \alpha F_{LSA}$ shown in red in **Figure S5**. The LSA force form (which is the same as the large distance HHF force) makes the transport equation tractable, but it has to be modified with the factor $\alpha = 1.6$ here to have a reasonable agreement with the simulations for the distances $\kappa y < 2$ of interest in the first capture phase.

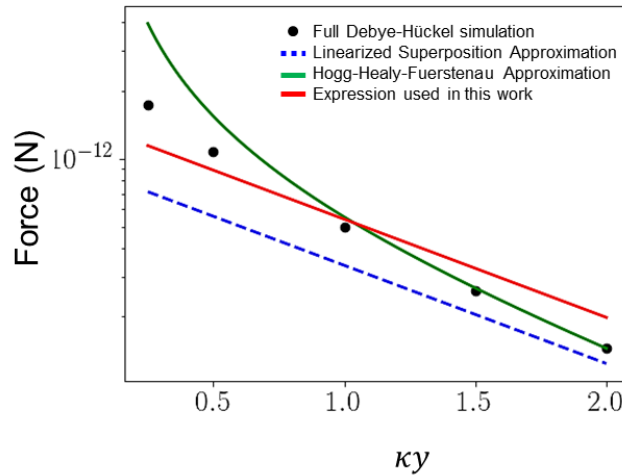


Figure S5. Particle-substrate electrostatic force as a function of distance for an isolated particle. The parameters are those used in the article. Black symbols: full Debye-Hückel simulation of one particle and a charged wall; Green curve: Derjaguin approximation (1); Blue dashed line: Linearized Superposition Approximation (2); Red line: expression used in this article (3).

Collective diffusion coefficient calculations

The value of the collective diffusion coefficient can be calculated with the generalized Stokes-Einstein relation $D = D_0 f / \chi$ where f is the sedimentation hindrance function and χ is the osmotic compressibility. For the hydrodynamically dilute dispersions considered here $f \approx 1$. As the mean surface to surface distance between particles in the bulk is at most $l_{s-s} \approx d \left(\phi^{-\frac{1}{3}} - 1 \right) = 1.7l_D$ in the simulations presented here, with ϕ the volume fraction, electric double layers interact everywhere and the osmotic compressibility can be calculated accurately with the cell model^{6,7}. For the system considered in **Figure 2b**, we obtain $D \in [220D_0, 245D_0]$.

Influence of the particle concentration

Figure S6 shows the $1\mu\text{m}$ normalized pattern and background particle densities of assemblies made by convective nanoxerography at different concentrations from $\rho_0/5$ to $2\rho_0$ where $\rho_0=6.825\times 10^8\text{ mL}^{-1}$. The static contact time was set to 0, with a dragging speed at $8\mu\text{m}\cdot\text{s}^{-1}$ leading to $t_{tc} = 275\text{s}$.

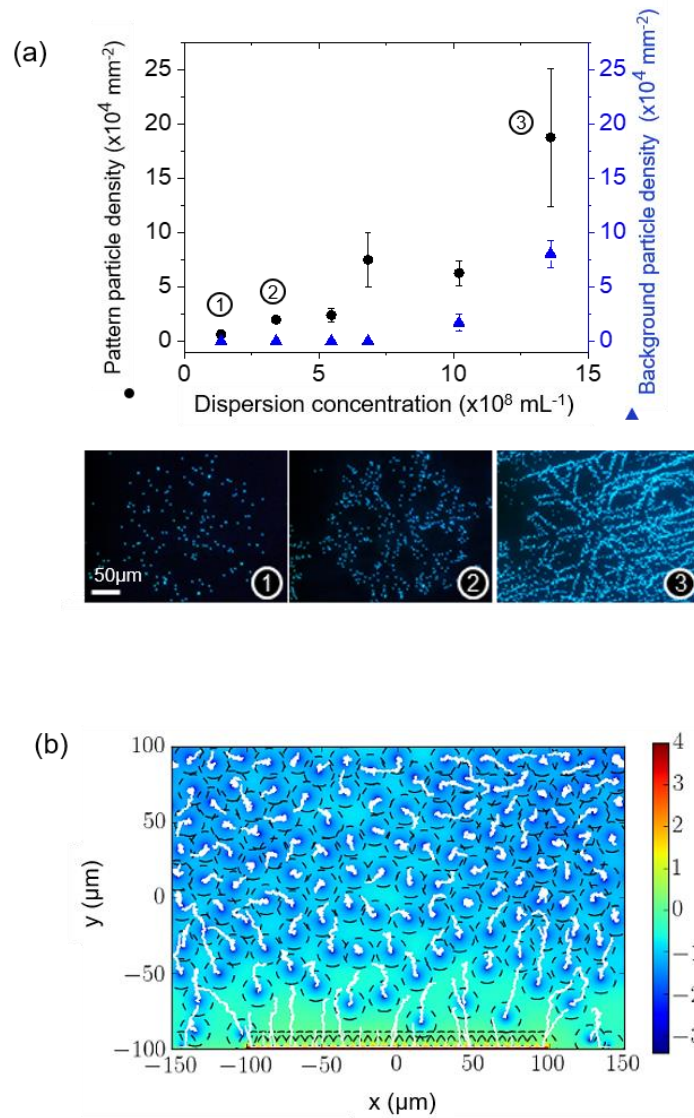


Figure S6. (a) Pattern and background particle densities as a function of the dispersion concentration for $1\mu\text{m}$ latex particles with fluorescent optical microscopy images of numbered assemblies, (b) Numerical simulations of particles trajectories above the charged pattern. The electrostatic potential field is the one obtained for the final simulation time. The bulk particle density is $\rho_b = 1.37 \times 10^9\text{ mL}^{-1}$

Both densities are increasing with the dispersion concentration, a conclusion that has also been reported in the case of smaller particles assembled by nanoxerography.⁸ Indeed, by extending the number of particles in the dispersion drop, the probability to locate some of them close

enough to the charged pattern to induce electrostatic attraction and the convective flux density ρu are both increased linearly. The numerical simulation configuration with a high number of particles presented on **Figure S6b** shows that particle screening lengths are recovering from one particle to another at such concentration which makes the effective diffusion coefficient D increase by coulombic repulsions. The negatively charged particles quickly deposited onto the charged pattern, by electrostatic attraction in the area $y < l_D$, do not screen the electric potential generated by the positive patterns which allows the deposition of additional particles and the pattern particle density increase by carrying on the development.

Finally, a working concentration of $\rho_b = 6.825 \times 10^8$ Ps/mL gives a pattern particle density high enough with a good selectivity.

Influence of the substrate temperature

An analysis of the influence of the substrate temperature on $1\mu\text{m}$ particles assemblies has also been done. Results are shown in **Figure S7**.

Pattern and background particle densities increase with the substrate temperature from a threshold $T_{\text{th}} = 20^\circ\text{C}$. By using real-time optical microscopy recordings, one can see that the convective flow rate speeds up for temperatures higher than T_{th} . The solvent evaporation rate increases with the temperature difference between the top of the drop, corresponding to the room temperature, and the edge of the drop,⁹ the temperature of the heated substrate. For the range of temperatures investigated (17 to 25°C), the vapor pressure increases roughly by a factor two. Consequently, the solvent evaporation rate directly increases with the substrate temperature and makes the convective flow speed up, which increases the particle flux towards the triple line. In addition, the viscosity of the solvent heated by the substrate diminishes by about 30%, and the particle diffusion coefficient D_0 increases by about 30%. Both phenomena facilitate particle displacements to the edge of the meniscus. A working temperature just below T_{th} prevents the predominance of convective flow effects and allows the analysis of other parameters.

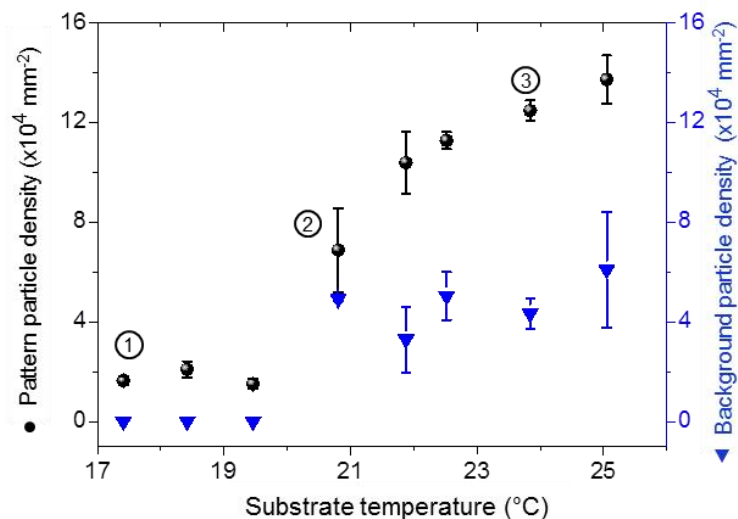


Figure S7. 1 μm latex particle pattern and background densities as a function of the stage temperature and fluorescent optical microscopy images of numbered assemblies.

Initial contact time influence on the convective flow assembly of 500nm and 4.3 μm

The initial contact time influence on the assembly of 500 nm and 4.3 μm latex particles assembled by a convective flow development method was analyzed as for the 1 μm particles. **Figures S8 and S9** present the corresponding results.

The experimental curve for the 500 nm particles was fitted with a function $f(t) = At^b$, where $A = 3220 \pm 179 \text{ Ps. mm}^{-2}$ and $b = 0.40 \pm 0.01$. The shape of the fitting curve is close to a $\sim \sqrt{t}$ function pointing out a diffusion mechanism.

Fitting correctly a $\sim \sqrt{t}$ function was not possible for the 4.3 μm particles. It might be because of the sedimentation phenomenon involved in their assembly. Indeed, their sedimentation speed is about 18 times higher than that of 1 μm particles. In addition, 4.3 μm particles are more likely to roll on the substrate surface to move towards or away from charged patterns due to electrostatic or hydrodynamic forces.

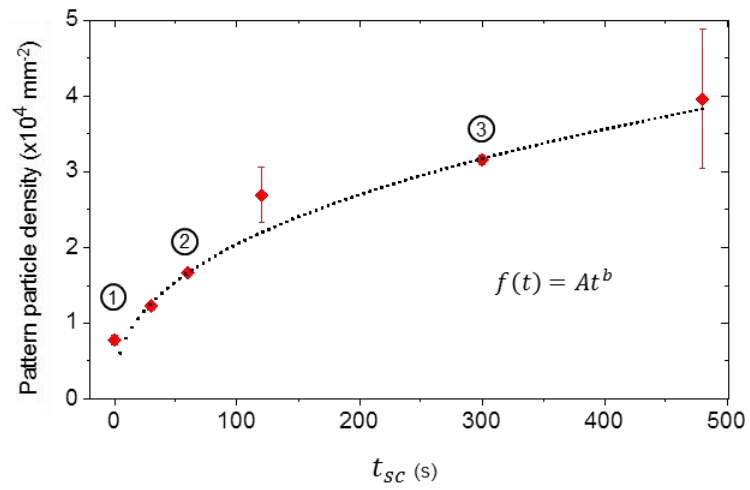


Figure S8. Pattern particle density as a function of the static contact time t_{sc} before the 500 nm latex dispersion drop dragging and fluorescent optical microscopy images of numbered assemblies.

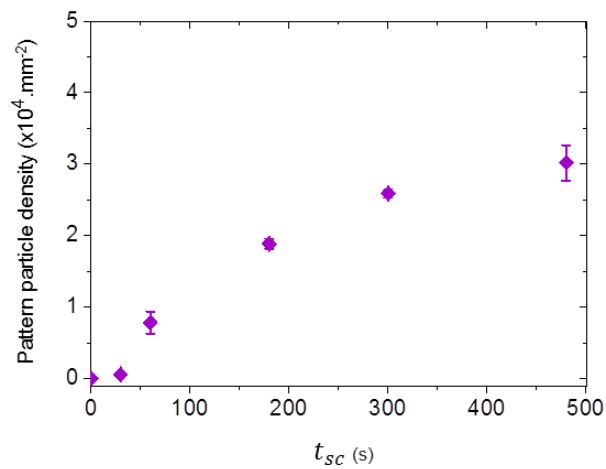


Figure S9. Pattern particle density as a function of the static contact time t_{sc} with a dragging speed of $80 \mu\text{m}\cdot\text{s}^{-1}$ for $4.3 \mu\text{m}$ latex particles

REFERENCES

- (1) Teulon, L.; Palleau, E.; Morales, D.; Poirot, D.; Ressier, L. Interactive Nanogel Marking at the Microscale for Security and Traceability Applications. *Adv. Mater. Technol.* **2018**, *3*, 1700244.
- (2) Cau, J.-C.; Ludovic, L.; Marie, N.; Adriana, L.; Vincent, P. Magnetic Field Assisted Microcontact Printing: A New Concept of Fully Automated and Calibrated Process. *Microelectron. Eng.* **2013**, *110*, 207–214.
- (3) Ohshima, H. Electrophoretic Mobility of Spherical Colloidal Particles in Concentrated Suspensions. *J. Colloid Interface Sci.* **1997**, *188*, 481–485.
- (4) Bell, G. M.; Levine, S.; McCartney, L. N. Approximate Methods of Determining the Double-Layer Free Energy of Interaction between Two Charged Colloidal Spheres. *J. Colloid Interface Sci.* **1970**, *33*, 335–359.
- (5) Hogg, R.; Healy, T. W.; Fuerstenau, D. W. Mutual Coagulation of Colloidal Dispersions. *Trans. Faraday Soc.* **1966**, *62*, 1638–1651.
- (6) Hallez, Y.; Diatta, J.; Meireles, M. Quantitative Assessment of the Accuracy of the Poisson–Boltzmann Cell Model for Salty Suspensions. *Langmuir* **2014**, *30*, 6721–6729.
- (7) Deserno, M.; Holm, C. Cell Model and Poisson-Boltzmann Theory: A Brief Introduction. *ArXivcond-Mat0112096* **2001**.
- (8) Sangeetha, N. M.; Moutet, P.; Lagarde, D.; Sallen, G.; Urbaszek, B.; Marie, X.; Viau, G.; Ressier, L. 3D Assembly of Upconverting NaYF₄ Nanocrystals by AFM Nanoxerography: Creation of Anti-Counterfeiting Microtags. *Nanoscale* **2013**, *5*, 9587.
- (9) Bhardwaj, R.; Longtin, J. P.; Attinger, D. Interfacial Temperature Measurements, High-Speed Visualization and Finite-Element Simulations of Droplet Impact and Evaporation on a Solid Surface. *Int. J. Heat Mass Transf.* **2010**, *53*, 3733–3744.